Surfactant micelle self-assembly directed highly symmetric ultrasmall inorganic cages

Authors: Kai Ma[1], Yunye Gong[2], Tangi Aubert[1,3], Melik Z. Turker[1], Teresa Kao[1], Peter C. Doerschuk[2,4], Ulrich Wiesner[1]

Affiliations:

[1]Department of Materials Science Engineering, Cornell University, Ithaca, NY 14853, USA.

[2] School of Electrical and Computer Engineering, Cornell University, Ithaca, NY, 14853, USA.

[3]Department of Chemistry, Ghent University, Ghent, 9000, Belgium.

[4]Nancy E. and Peter C. Meinig School of Biomedical Engineering, Cornell University, Ithaca, NY 14853, USA.

Correspondence to: Ulrich Wiesner (ubw1@cornell.edu)

Nanoscale objects with highly symmetrical cage-like polyhedral shapes, often with icosahedral symmetry, have recently been assembled using DNA[1-3], RNA[4], and proteins[5,6] for biomedical applications. These achievements relied on advances in the development of programmable self-assembling biomaterials[7-10], as well as rapidly developing single-particle three-dimensional (3D) reconstruction techniques of cryo electron microscopy (cryo-EM) images that provide high-resolution structural characterization of biological complexes[11-13]. In contrast, such single-particle 3D

reconstruction approaches have not been successfully applied to help identify unknown synthetic inorganic nanomaterials with highly symmetrical cage-like shapes. In this paper, employing a combination of cryo-EM and single-particle 3D reconstruction, we suggest the existence of isolated ultrasmall silica cages ("silicages") with dodecahedral structure. We hypothesize that this highly symmetric self-assembled cage forms via arrangement of primary silica clusters in aqueous solutions on the surface of oppositely charged surfactant micelles. This discovery paves the way for such nanoscale cages from silica and other inorganic materials to be used as building blocks for a wide range of advanced functional materials applications.

For the search of dodecahedral silica cage structures (Figure 1), we looked at the early formation stages of surfactant micelle directed silica self-assembly[14]. Our synthesis system contained cetyltrimethylammonium bromide (CTAB) surfactant micelles and tetramethyl orthosilicate (TMOS) as a sol-gel silica precursor (see Methods section). Hydrophobic mesitylene (TMB) was added into the aqueous CTAB micelle solution, increasing micelle size and deformability[15]. TMOS was selected as the silica source due to its fast hydrolysis rate in water, and the initial reaction pH was adjusted to ~8.5. Following TMOS addition, its hydrolysis to silicic acid reduced the reaction pH to neutral[16,17]. The lowered pH accelerated silane condensation, forming primary silica clusters with diameter around 2 nm[18]. The negatively charged silica clusters were attracted to the positively charged CTAB micelle surface, assembling into micelle templated nanostructures[14]. This experimental design, where fast hydrolysis and

condensation of the silica precursor quickly terminated the reaction process, allowed preservation of early formation stages of micelle directed silica self-assembly[17].

In order to improve particle dispersity on transmission electron microscopy (TEM) grids, low molar mass silane modified monofunctional polyethylene glycol (PEG) was added into the solution one day prior to TEM sample preparation, thereby covalently coating the accessible silica surface[19], yielding PEGylated nanoparticles (Extended Data Figure 1) that could be further purified and isolated from the synthesis solution. Narrowly size distributed particles were observed under TEM with average diameter around 12 nm (Figure 2a and inset), consistent with silica structures wrapped around TMB swollen CTAB micelles[15]. The detailed particle structure was difficult to identify, however. Therefore, TEM samples were subsequently plasma etched on carbon grids for five seconds prior to imaging to remove excess organic chemicals (*e.g.* PEG-silane), otherwise contributing to background noise. To further improve the signal-to-noise ratio, a series of images were acquired of the same sample area and averaged. Stripes and windows in zoomed-in images of individual particles became more clearly recognizable, suggesting the presence of cage-like structures (Figure 2b and insets).

The study of thousands of such single particle TEM images revealed the prevalence of two cage projections with two- and, in particular, five-fold symmetry, respectively (Figure 2c), too few to allow for a successful 3D reconstruction. We therefore shifted our attention to cryo-EM characterization of the native reaction solution. The silica surface PEGylation step was omitted as the high PEG concentration substantially increased radiation sensitivity of the samples, resulting in difficulties obtaining clear cryo-EM images.

Cryo-EM provided direct visualization of particles in solution with arbitrary orientation, *i.e.* without disturbances due to sample drying on TEM substrates, including structure deflation. The background noise was significantly reduced as a result of the absence of a TEM substrate as well as chemicals dried onto the substrate during sample preparation (Figure 2c). Although particle aggregation was occasionally observed in cryo-EM (Figure 2d), individual silica nanoparticles with cage-like structures could always be identified (Figure 2c and d). No particle aggregation was observed in dry-state TEM of PEGylated particles, suggesting that particle aggregation observed by cryo-EM was a reversible process that could be overcome via insertion of PEG chains.

We manually identified ~19,000 single particle images from cryo-EM micrographs, clustered them and averaged the images in each cluster in order to improve the signal-to-noise ratio[20]. The averages showed different orientations of silica nanoparticles with cage-like structures, *i.e.* silicages (Extended Data Figure 2a). Averages were identified that were consistent with selected projections of a pentagonal dodecahedral cage (Figure 2c and Extended Data Figure 2b). The dodecahedral silicage (icosahedral point group, I^h, Figure 1) is the simplest of a set of Voronoi polyhedra suggested to form the smallest structural units of multiple forms of mesoporous silica[21]. Although such highly symmetric ultrasmall silica cages have never been isolated before, it seemed likely that this should be possible.

Guided by this structural insight, single-particle 3D reconstruction of silicages were performed using the "Hetero"[22] model-based maximum likelihood algorithm, in which a two-class reconstruction was computed to overcome challenges associated with structural heterogeneity (Methods section) and rotational icosahedral symmetry was

imposed on both classes (Extended Data Figure 2). One of the two-class reconstructions was a dodecahedral cage (Figure 3a and b). Low intensity signal was identified inside the reconstructed cage, consistent with the presence of TMB swollen CTAB micelles inside the silicage, whose electron density is lower than silica but higher than the surrounding ice. The other class (*i.e.*, non-cage) did not provide an interpretable structure, likely due to heterogeneity in the structure of the corresponding particles. Such two-class reconstructions were performed using different numbers of single particle images (2000, 7000, and 10000) and yielded consistent results. Single-class reconstructions were also performed, using only the images in the class showing dodecahedral cages in two-class reconstructions, by the Hetero algorithm. Equivalent two-class and single-class reconstructions were also performed by the widely-used RELION 2.1[24] system. Dodecahedral cage structures were obtained in all these reconstructions (Extended Data Figure 3 and Supplementary Videos 1 and 2). The resolution of the reconstructions was approximately 2 nm[25] (Extended Data Figure 4). Silica in these cages is amorphous at the atomic level, which prevented atomic resolution in these reconstructions.

The Hetero reconstruction algorithm provided estimates of the projected orientation (*i.e.*, three Euler angles) for each experimental image, which were used to compute predicted projections. Nine predicted projections and corresponding experimental images were manually clustered, and averages were computed for each cluster (Figure 3c). The similarity of the projections of the 3D reconstruction and the averaged experimental images supports the dodecahedral cage structure. Furthermore, the theoretical probabilities of finding each of the nine projections (Figure 3c) were calculated based on the assumption that the orientations of silicages in cryo-EM are

113 random. The results were then compared to the probabilities observed by single particle
114 3D reconstruction (Extended Data Figure 5). The high consistency between theoretical
115 and experimental projection probabilities further supports the dodecahedral cage
116 reconstruction.

117 While at this early point we can only speculate about the exact formation
118 mechanism of the observed silicage structure, there are clues found in the details of the
119 reconstruction. The vertices of the dodecahedral silicage had a diameter around 2.4 nm
120 (Figure 3b), only slightly larger than the diameter of primary silica clusters, *i.e.* ~2 nm[18]
121 (Extended Data Figure 6). The interstitial spacing between two nearby vertices was
122 estimated to be about 1.4 nm (*i.e.,* edge length, 3.8 nm, minus diameter of vertices, 2.4
123 nm, see Figure 3b), much smaller than the diameter of such clusters. Bridges between
124 vertices forming the edges of the dodecahedron were substantially thinner than the size of
125 the primary clusters (Figure 3a and b). This suggests that negatively charged primary
126 silica clusters formed in solution may start to come down onto the positively charged
127 micelle surface attracted by Coulomb interactions. As more and more silica clusters
128 assemble on the micelle surface, as a result of their repulsive interactions and possible
129 interactions with other micelles, they may move to the vertices of a dodecahedron.
130 Additional silane condensation onto the surface of growing clusters may eventually lead
131 to bridge formation resulting in the final observed cage structure (Figure 3). The origin of
132 icosahedral symmetry in viruses has been associated with the energy minimization of two
133 opposing interactions, repulsive interactions associated with the bending rigidity and
134 attractive hydrophobic interactions[27]. In a related way, in addition to electrostatic
135 interactions, deformation of the micelle surface around the silica clusters may be another

136 important contributor to the free energy in our system. This is supported by experiments
137 showing that the cage structures do not form in the absence of TMB (Extended Data
138 Figure 7), which is expected to enhance micelle surface deformability.

139 Micelle self-assembly directed ultrasmall cage structures could also be fabricated
140 from other inorganic materials with similar feature sizes and surface chemistry
141 characteristics to silica. In preliminary experiments silica was replaced by two metals,
142 gold and silver, and a transition metal oxide, vanadium oxide. Gold and silver structures
143 were prepared by the reduction of metal precursors, $HAuCl_4 \cdot 3H_2O$ and $AgNO_3$,
144 respectively, in the presence of the micelles (Extended Data Figure 8, also see Methods
145 section). Tetrakis(hydroxymethyl)phosphonium chloride (THPC) was used as both the
146 reductant and the capping agent to stabilize primary gold and silver nanoparticles and
147 provide negative surface charges[28]. In contrast, primary vanadium oxide nanoparticles
148 with native negatively charged particle surface were prepared via sol-gel chemistry[29],
149 similar to the synthesis of silicages (Methods section). Images of individual particles
150 obtained by TEM revealed similar internal structure (Figure 4). These nanoparticles did
151 not appear to be dense but instead showed cage-like structures (compare Figure 2 and 4),
152 further corroborated by associated projection averages[20] revealing cages with rotational
153 symmetry (bottom insets in Figure 4), similar to the prevalent projection in case of the
154 silicage (*vide supra*). Micelle self-assembly directed cages like the dodecagonal structure
155 described in this paper may therefore not be unique to amorphous silica, but may provide
156 direct synthesis pathways to crystalline material cages (Extended Data Figure 9).

157 There are a number of important ramifications that derive from our silicage
158 discovery. For example, such cages are considered as individual structural units from

which larger scale mesoporous silica is built up in a bottom-up manner[15,21]. However, since a dodecahedron cannot be used to generate a tessellation of 3D space, other silica cage structures would be required. This motivates better understanding of early formation pathways of surfactant directed silica self-assembly, including the search for micelle directed ultrasmall silicages with other structures, and from other materials (*vide supra*). Furthermore, the chemical and practical value of this polyhedral structure may prove extremely high. Considering the high versatility of silica surface chemistry, and the ability to distinguish cage inside and outside via micelle directed synthesis[17], one can readily conceive cage derivatives of many kinds, which may exhibit unusual properties and be useful in applications ranging from catalysis to drug delivery. For example, based on recent successes in clinical translation of ultrasmall fluorescent silica nanoparticles with similar particle size and surface properties [30], a whole range of novel diagnostic and therapeutic probes with drugs hidden in the inside of the cages can be envisaged.

1. He, Y. *et al.* Hierarchical self-assembly of DNA into symmetric supramolecular polyhedra. *Nature* **452,** 198–201 (2008).
2. Douglas, S. M. *et al.* Self-assembly of DNA into nanoscale three-dimensional shapes. *Nature* **459,** 1154–1154 (2009).
3. Iinuma, R. *et al.* Polyhedra self-assembled from DNA tripods and characterized with 3D DNA-PAINT. *Science* **344,** 65–69 (2014).
4. Afonin, K. A. *et al.* In vitro assembly of cubic RNA-based scaffolds designed in silico. *Nat. Nanotechnol.* **5,** 676–682 (2010).
5. King, N. P., Sheffler, W., Sawaya, M. R., Vollmar, B. S., Sumida, J. P., André, I., Gonen, T., Yeates, T. O., Baker, D. Computational design of self-assembling protein nanomaterials with atomic level accuracy. *Science **336***, 1171–1174 (2012).
6. Hsia, Y. *et al.* Design of a hyperstable 60-subunit protein icosahedron. *Nature* **535,** 136–150 (2016).
7. Rothemund, P. W. Folding DNA to create nanoscale shapes and patterns. *Nature* **440**, 297–302 (2006).
8. Yin, P., Choi, H. M. T., Calvert, C. R., Pierce, N. A. Programming biomolecular self-assembly pathways. *Nature* **451**, 318–322 (2008).
9. Ke, Y., Ong, L., Shih, W., Yin, P. Three-dimensional structures self-assembled from DNA bricks. *Science* **338**, 1177–1183 (2012).

10. King, N. P. et al. Accurate design of co-assembling multi-component protein nanomaterials. *Nature* **510**, 103–108 (2014).
11. Zhao, M., Wu, S., Zhou, Q., Vivona, S., Cipriano, D. J., Cheng, Y., Brunger, A. T. Mechanistic insights into the recycling machine of the SNARE complex. *Nature.* **518**, 61–67 (2015).
12. Fernandez-Leiro, R. & Scheres, S. H. W. Unravelling biological macromolecules with cryo-electron microscopy. *Nature* **537,** 339–346 (2016).
13. Dai, X., Li, Z., Lai, M., Shu, S., Du, Y., Zhou, Z. H., Sun, R. In situ structures of the genome and genome-delivery apparatus in a single-stranded RNA virus. *Nature* **541**, 112–116 (2017).
14. Kresge, C. T., Leonowicz, M. E., Roth, W. J., Vartuli, J. C. & Beck, J. S. Ordered mesoporous molecular sieves synthesized by a liquid-crystal template mechanism. *Nature* **359,** 710–712 (1992).
15. Sun, Y. *et al.* Formation pathways of mesoporous silica nanoparticles with dodecagonal tiling. *Nat. Commun.* **8,** 252 (2017).
16. Ma, K. *et al.* Control of ultrasmall sub-10 nm ligand-functionalized fluorescent core–shell silica nanoparticle growth in water. *Chem. Mater.* **27,** 4119–4133 (2015).
17. Ma, K., Sai, H. & Wiesner, U. Ultrasmall sub-10 nm near-infrared fluorescent mesoporous silica nanoparticles. *J. Am. Chem. Soc.* **134,** 13180–13183 (2012).
18. Carcouët, C. C. M. C., Van De Put, M. W. P., Mezari, B., Magusin, P. C. M. M., Laven, J., Bomans, P. H. H., Friedrich, H., Esteves, A. C. C., Sommerdijk, N. A. J. M.; Van Benthem, R. A. T. M., With, G. D. Nucleation and growth of monodisperse silica nanoparticles. *Nano Lett.* **14**, 1433–1438 (2014).
19. Ma, K., Zhang, D., Cong, Y. & Wiesner, U. Elucidating the mechanism of silica nanoparticle PEGylation processes using fluorescence correlation spectroscopies. *Chem. Mater.* **28,** 1537–1545 (2016).
20. Tang, G., Peng, L., Baldwin, P. R., Mann, D. S., Jiang, W., Rees, I. & Ludtke, S. J. EMAN2: An extensible image processing suite for electron microscopy. *J. Struct. Biol*. **157,** 38-46 (2007).
21. Xiao, C., Fujita, N., Miyasaka, K., Sakamoto, Y. & Terasaki, O. Dodecagonal tiling in mesoporous silica. *Nature* **487,** 349–353 (2012).
22. Gong, Y., Veesler, D., Doerschuk, P. C. & Johnson, J. E. Effect of the viral protease on the dynamics of bacteriophage HK97 maturation intermediates characterized by variance analysis of cryo EM particle ensembles. *J. Struct. Biol.* **193,** 188–195 (2016).
23. Goddard, T. D., Huang, C. C., Couch, G. S., Greenblatt, D. M., Meng, E. C., and Ferrin, T. E. UCSF Chimera-A visualization system for exploratory research and analysis. *J. Comput. Chem*. **25,** 1605-1612 (2004).
24. Scheres, Sjors H.W. RELION: Implementation of a Bayesian approach to cryo-EM structure determination. *J.Struct. Biol.* **180**, 519-530 (2012).
25. Harauz, G. and van Heel, M. Exact filters for general geometry three dimensional reconstruction. *Optik* **73,** 146-156 (1986). Eq. 17.
26. Rohou, A. and Grigorieff, N. CTFFIND4: Fast and accurate defocus estimation from election micrographs. *J.Struct. Biol.* **192**, 216-221 (2015).
27. Zandi, R., Reguera, D., Bruinsma, R. F., Gelbart, W. M. & Rudnick, J. Origin of icosahedral symmetry in viruses. *Proc. Natl Acad. Sci. USA* **101,** 15556–15560 (2004).
28. Duff, D. G., Baiker. A., Edwards, P. P. New hydrosol of gold clusters. 1. Formation and particle size variation. *Langmuir* **9**, 2301-2309 (1993).
29. Sullivan, L. M., Li, L. & Lukehart, C. M. Synthesis of VO2 Nanopowders. Part I. Sol–Gel Processing of Vanadium Alkoxide Precursor Within Inverse Micelles. *J. Clust. Sci.* **25,** 313–322 (2013).

30. Phillips, E.; Penate-Medina, O.; Zanzonico, P. B.; Carvajal, R. D.; Mohan, P.; Ye, Y.; Humm, J.; Gonen, M.; Kalaigian, H.; Schoder, H.; *et al.* Clinical translation of an ultrasmall inorganic optical-PET imaging nanoparticle probe. *Sci. Transl. Med.* **6**, 260ra149 (2014**)**.

Supplementary Information is available in the online version of the paper.

Acknowledgments This project was support by the National Cancer Institute of the National Institutes of Health under Award Number U54CA199081. Y.G. and P.C.D. gratefully acknowledge financial support by the National Science Foundation under grant number 1217867, and Y.G. gratefully acknowledges financial support by a 2017 Google Ph.D. Fellowship in Machine Learning. T.A. acknowledges financial support by the Ghent University Special Research Fund (BOF14/PDO/007) and the European Union's Horizon 2020 research and innovation program (MSCA-IF-2015-702300). M.Z.T. gratefully acknowledges fellowship support by the Ministry of National Education of the Republic of Turkey. Work made use of shared facilities of the Cornell Center for Materials Research (CCMR) with funding from the NSF MRSEC program (DMR-1719875), and the Nanobiotechnology Center shared research facilities at Cornell. The authors gratefully thank V. Elser and Y. Jiang, Cornell Physics Department, for helpful discussions.

Author Contributions K.M., T.A. and U.W. designed the experimental work. Y.G. and P.C.D. performed the reconstructions. K.M. synthesized the silica-based materials. T.A. synthesized the metal and transition metal oxide based materials. K.M. and T.A. performed TEM and cryo-EM characterizations. K.M., T.A., M.T., and T.K. processed the images for reconstructions. K.M., T.A., and U.W. discussed the experimental work. U.W. wrote the manuscript with input of all coauthors. U.W. supervised the work.

Author Information Reprints and permissions information is available at www.nature.com/reprints. A patent disclosure based on this study has been filed through Cornell University. Readers are welcome to comment on the online version of this article at www.nature.com/nature. Correspondence and requests for materials should be addressed to U. W. (ubw1@cornell.edu).

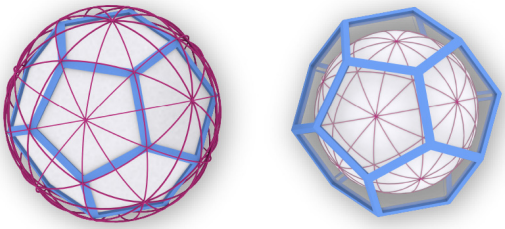

Figure 1 | Representation of dodecahedron. Among the platonic solids, the dodecahedron best fills out its circumscribed sphere, *i.e.* a sphere that passes through all its vertices (left). The inscribed sphere passing through all facets (right) is shown for comparison.

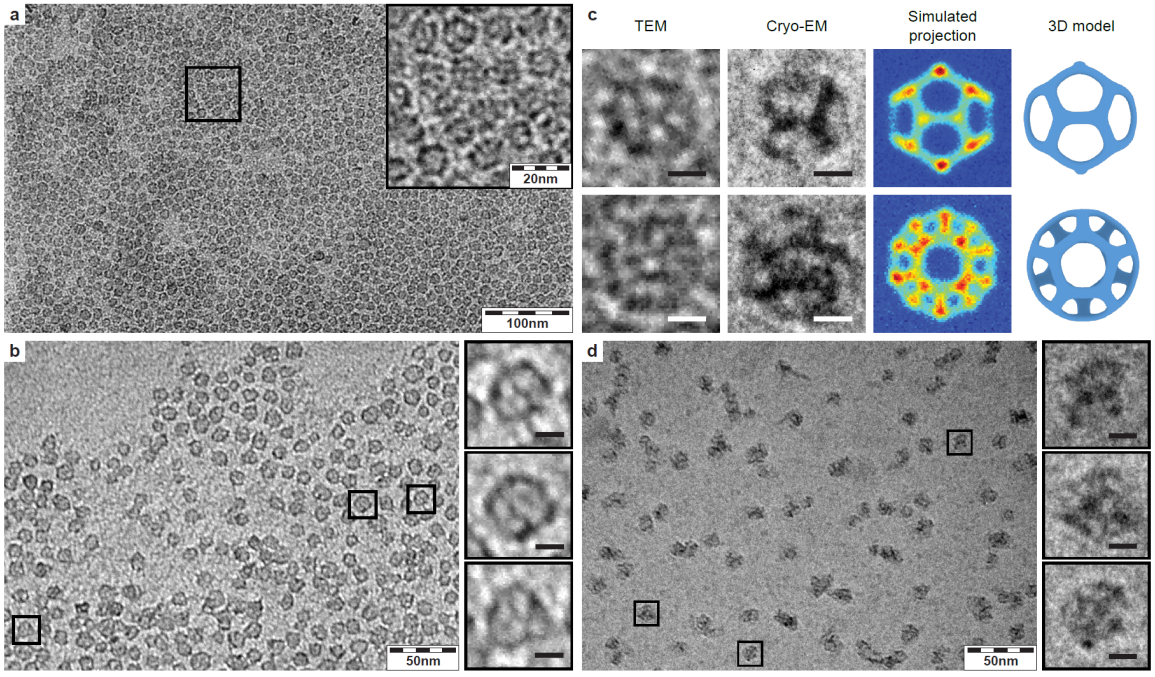

Figure 2 | TEM and cryo-EM characterizations of silicages. a, TEM images at low magnification of PEG-coated silicages on carbon substrate. The inset in (**a**) shows a zoomed-in image. **b**, Averaged TEM image using eleven images acquired of the same sample area of PEG-coated silicages with insets showing representative individual structures at higher magnification. The sample was plasma etched for five seconds prior to TEM characterization to reduce background noise. **c**, Comparison between silicages observed in TEM and cryo-EM with projections of simulated dodecahedral cages and models. **d**, Cryo-EM images of silicages without PEG coating. Scale bars in the insets in (**b**, **c** and **d**) are 5 nm.

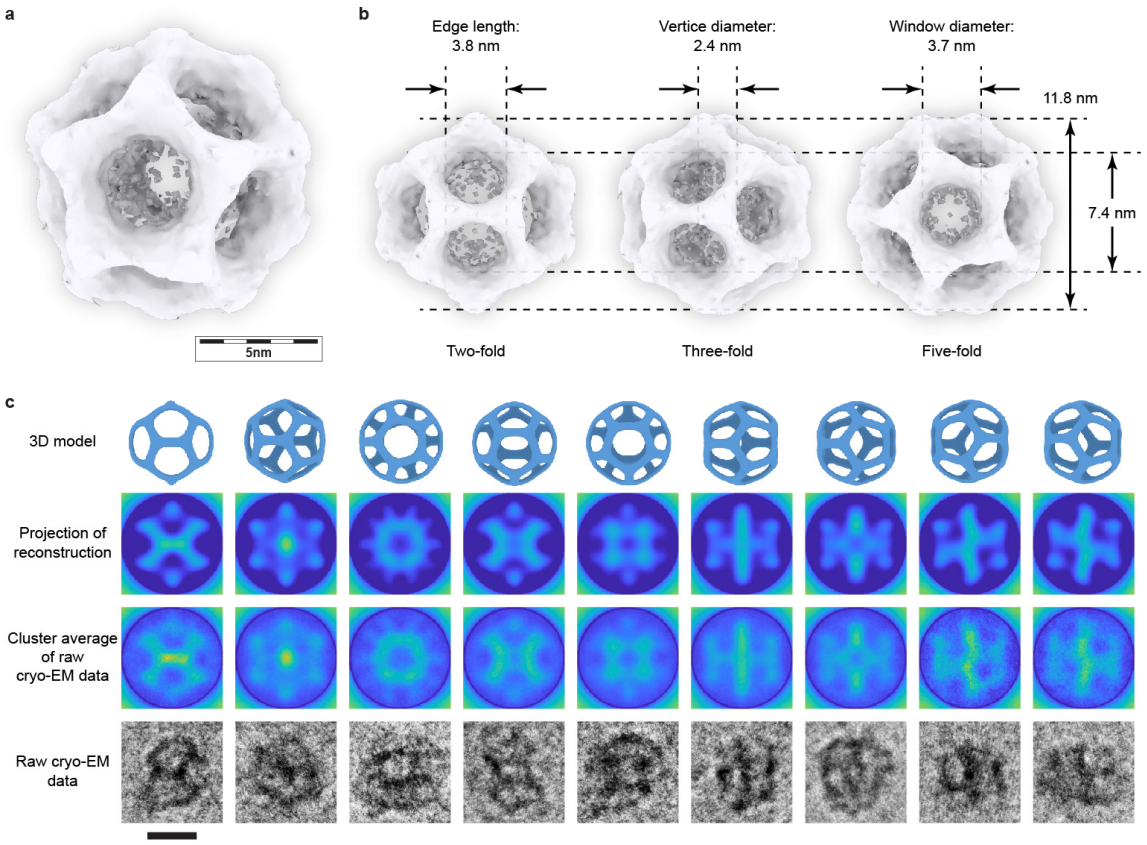

Figure 3 | Single particle reconstruction of dodecahedral silicage. **a** and **b**, Dodecahedral silicage reconstruction result (**a**) and its three most unique projections along the two-, three- and five-fold symmetry axes (**b**). The average dimensions of silicages were estimated based on the reconstructed dodecahedral silicage (**b**). **c**, Representative comparison of nine unique projections from the reconstruction and cryo-EM cluster averages with projections of a 3D dodecahedral cage model (top row in **c**). Corresponding single cryo-EM images are displayed at the bottom in (**c**) highlighting the difference between raw data and reconstruction. Scale bar in (**c**) is 10 nm. Visualizations in panels (**a**) and (**b**) are by UCSF Chimera[23].

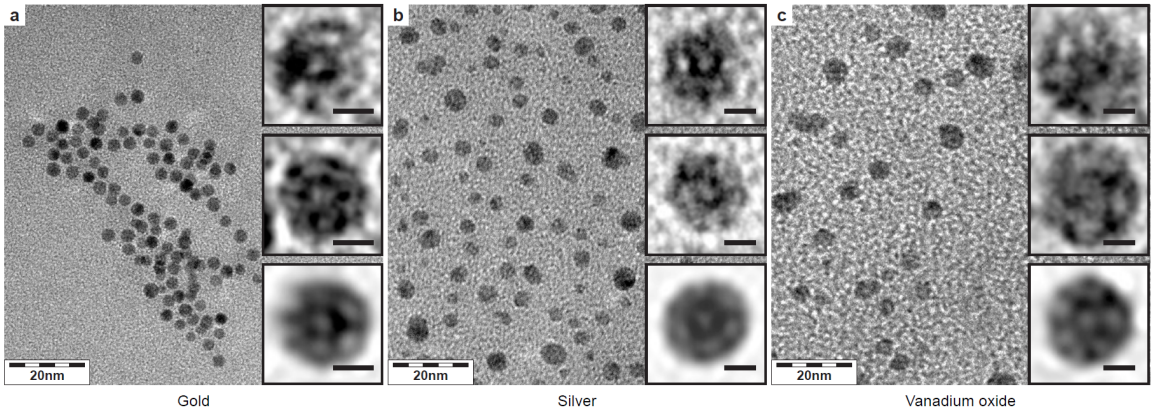

Figure 4 | Cage-like structures with different inorganic compositions. **a**, **b**, and **c**, Similar cage-like nanoparticles were obtained when silica was replaced by other

materials, including gold (**a**), silver (**b**), and vanadium oxide (**c**). The insets display zoomed-in images of individual particles (top two rows) and averaged images[20] (bottom row). The scale bars in all insets are 2 nm.

METHODS

Chemicals and materials. All chemicals were used as received. Cetyltrimethylammonium bromide (CTAB), ammonia (2 M in ethanol), mesitylene (1,3,5 trimethylbenzene, TMB), tetramethyl orthosilicate (TMOS), gold chloride trihydrate ($HAuCl_4 \cdot 3H_2O$), silver nitrate ($AgNO_3$), tetrakis(hydroxymethyl)phosphonium chloride (THPC), dimethyl sulfoxide (DMSO), acetic acid, and ethanol were purchased from Sigma-Aldrich. Vanadium oxytriisopropoxide was purchased from Alfa Aesar. Anhydrous potassium carbonate (K_2CO_3) was purchased from Mallinckrodt. Anhydrous ethanol was purchased from Koptec. Silane modified monofunctional polyethylene glycol (PEG-silane) with molar mass around 500 g/mol (6-9 ethylene glycol units) was purchased from Gelest. Carbon film coated copper grids for TEM and C-Flat holey carbon grids for cryo-EM were purchased from Electron Microscopy Sciences.

Synthesis, TEM, and cryo-EM characterization of silicages. Silicages were synthesized in aqueous solution through surfactant directed silica condensation. 125 mg of CTAB was first dissolved in 10 ml of ammonium hydroxide solution (0.002 M). 100 µl of TMB was then added to expand CTAB micelle size, and the water: CTAB: TMB molar ratio was about 1620: 1: 2. The solution was stirred at 600 rpm at 30 °C overnight, followed by the addition of 100 µl of TMOS. The reaction was then left at 30 °C overnight under stirring at 600 rpm.

To prepare cryo-EM samples, 5 µl of the native reaction solution was applied to glow discharged CF-4/2-2C Protochips C-Flat holey carbon grids, blotted using filter paper and plunged into a liquid mixture of 37% ethane and 63% propane at -194 °C using an EMS

plunge freezer. Cryo-EM images were acquired on a FEI Tecnai F20-ST TEM operated at an acceleration voltage of 200 kV using a Gatan Orius CCD camera. All cryo-EM images used for reconstruction were acquired at the same magnification, with a pixel size of 0.16 nm, and nominal defocus was kept between 1 μm and 2 μm.

To prepare dry-state TEM samples, 100 μl of PEG-silane was added into the reaction solution. The reaction solution was left at 30 °C overnight under stirring at 600 rpm to surface modify silicages covalently with PEGs to improve their dispersity on TEM grids. Afterwards, 30 μl of the reaction solution was dropped onto a cupper grid coated with a continuous carbon film, and blotted using filter paper. TEM images were acquired using a FEI Tecnai T12 Spirit microscope operated at an acceleration voltage of 120 kV. In order to improve the signal to noise ratio in recorded images, TEM sample grids were plasma etched for 5 seconds before TEM characterization, and a series of images was acquired of the same sample area, which was then averaged.

In order to quench individual primary silica clusters formed at the very early stages of cage formation, 100 μl of PEG-silane was added into the reaction solution about three minutes after the addition of TMOS. The rest of the procedures, including particle synthesis, dry-state TEM sample preparation, and TEM characterization, were the same as described above.

Particle purification. To remove CTAB and TMB from the cages, after adding PEG-silane and stirring at room temperature for a day (Methods section), the solution was heat-treated at 80 °C overnight to further enhance the covalent attachment of PEG-silane to the silica surface of the silicages. The PEGylated nanocages were first dialyzed

(molecular weight cut off, MWCO, 10 kDa) in a mixture of acetic acid, ethanol, and water (volume ratio 7:500:500) for three days, and were then dialyzed in DI water for another three days[17]. In both cases the dialysis solutions were changed once per day. The dry-state TEM sample preparation and TEM characterization methods were the same as described in the Methods section.

Synthesis of particles without TMB. The synthesis and TEM characterization methods used for particles without TMB were identical to those with TMB as described in the Methods section, except that the TMB addition step was omitted.

Silicage surface area and yield of production. The specific surface area of the silicages was assessed by a combination of nitrogen sorption measurements and theoretical estimations. After PEGylated silicage synthesis and purification, particles were first up-concentrated using a spin filter (Vivaspin 20, MWCO 10 kDa) and dried at 60 °C. Particles were then calcined at 550°C for 6 hours in air. The production yield was then estimated via dividing the remaining weight after calcination, *i.e.* weight of inorganic silica, by the theoretical weight of silica, *i.e.* calculated based on the amount of silica source added into the synthesis. Nitrogen adsorption and desorption isotherms were acquired using a Micromeritics ASAP 2020 (Extended Data Figure 1c) yielding a specific surface area of 570 m^2/g using the Brunauer−Emmett−Teller (BET) method. For comparison, using the dodecahedral cage model with the dimensions from the reconstruction shown in Figure 3, a theoretical surface area of silicages was estimated to be around 790 m^2/g. Overestimation of the experimental value is consistent with expected losses of surface area during sample calcination.

Synthesis and TEM characterization of metal cage-like structures. The gold and silver cage-like structures were prepared by the reduction of metal precursors, $HAuCl_4 \cdot 3H_2O$ and $AgNO_3$, respectively, in the presence of micelles with the same water: CTAB: TMB ratio as for the silicage work. In a typical batch, 50 mg of CTAB was dissolved in 4 ml of water at 30 °C, then 40 µl of TMB and 200 µl of ethanol were added to the mixture. After stirring the reaction at 30 °C overnight at 600 rpm, 16 µl of either $HAuCl_4 \cdot 3H_2O$ (25 mM) or $AgNO_3$ (25 mM) was added, followed after 5 minutes by 8 µl of THPC (68 mM). After another 5 minutes, 6 µl of potassium carbonate (0.2 M) was finally added.

Dry-state TEM samples for gold and silver cage-like structures were prepared after one day and 6 hours of reaction, respectively, due to different reaction rates as described in the Methods section. In both cases, the samples were prepared by drying 8 µl of the native reaction mixture diluted three times in ethanol on a TEM grid in air overnight. In order to remove the thick CTAB layer before imaging, the grid was immersed in ethanol for 2 minutes and then dried in air. TEM images of metal cage-like structures were acquired using a FEI Tecnai T12 Spirit microscope operated at an acceleration voltage of 120 kV.

Synthesis and TEM characterization of vanadium oxide cage-like structures. The vanadium oxide cage-like structures were prepared based on sol-gel chemistry very similar to the silicages, using vanadium oxytriisopropoxide as the precursor. In a typical batch, 50 mg of CTAB was dissolved in 4 ml of water at 30 °C, then 40 µl of TMB was added to the mixture. After stirring the reaction at 30 °C overnight at 600 rpm, 50 µl of vanadium oxytriisopropoxide diluted in 100 µl of DMSO was added to the reaction.

Dry-state TEM samples for vanadium oxide cage-like structures were prepared after one day of reaction by drying on a TEM grid 8 µl of the native reaction mixture diluted 10 times in water. At such dilution, the amount of CTAB was low enough so that the TEM samples did not require any plasma cleaning or soaking in ethanol prior to imaging. The TEM images of vanadium oxide cages were acquired using a FEI Tecnai T12 Spirit microscope operated at an acceleration voltage of 120 kV.

Particle reconstruction. The "Hetero" model-based maximum likelihood algorithm[22] was used which can simultaneously estimate: (1) a reconstruction for each type of particle shown in the images, (2) the type of particle shown in each image, and (3) the projection orientation for each image. Such joint estimation is a central feature of the algorithm and is a natural approach to process data from complicated mixtures. The estimates in (2) and (3), which are based on 3D structure, are independent of the clustering of 2D images, which is based on pixel values (*e.g.*, Extended Data Figure 2). In addition to the Hetero algorithm, the widely used RELION 2.1[24] system was applied to compute equivalent two-class and single-class reconstructions. The images were corrected for the CTF by phase flipping.

Additional details and optical characterization of the metal and vanadium oxide based syntheses of cage-like structures. In contrast to the sol-gel reaction leading to the silicage, the gold and silver cage-like structures syntheses relied on reduction reactions. To this end, tetrakis(hydroxymethyl)phosphonium chloride (THPC) was used as it reacts in water at basic pH to form trimethoxyphosphine, which can play both the role of reductant and capping agent for the metal nanoparticles. THPC has been widely used for

the synthesis of ultra-small (< 3 nm) and negatively charged phosphine-stabilized gold nanoparticles[28]. These nanoparticles are often used as seeds for the subsequent growth of continuous gold shells on the surface of aminated silica nanoparticles thanks to their high affinity and binding efficiency with amine groups[31,32]. Alcohol was added to the reaction mixture in order to mimic the conditions of the silicage synthesis where methanol is formed upon hydrolysis of TMOS. Early stage preliminary experiments showed that resulting structures were less size dispersed when using ethanol in slightly higher concentration than the released methanol in the silicage synthesis. Gold and silver cage-like structure syntheses were performed at a much lower concentration ([Au] or [Ag] = 93.7 μM) as compared to the silicages ([Si] = 65.9 mM). Attempts at synthesizing gold and silver cages at higher concentrations resulted in much larger nanoparticles with no apparent internal structure.

Gold based synthesis. The addition of gold precursor to the reaction initially resulted in the formation of a pale yellow precipitate which turned into a clear, *i.e.* non-turbid, darker orange solution within a couple of minutes under stirring at 30 °C (see Extended Data Figure 8 for a survey of the absorption characteristics at each step of the synthesis). Since neither the precipitate nor the darker orange coloration was observed in the absence of CTAB, we attribute these observations to some interaction between the gold chloride anions and the ammonium groups of the CTAB. After the addition of THPC, the solution turned colorless within a couple of minutes, indicating that gold(III) had been reduced to gold(I). The subsequent transformation of THPC into trimethoxyphosphine by increasing the pH with the addition of potassium carbonate happened within the first hour of reaction (see also description for the case of silver below). However, the reduction from

gold(I) to gold(0) was found to be rather slow with the first hint of coloration appearing after 8 hours of reaction. After one day of reaction, the solution ended up exhibiting a brown coloration. This brown coloration was the signature of gold nanoparticles which are too small or not dense enough to show a strong surface plasmon resonance, as evidenced by the absorption profile in Extended Data Figure 8 which only shows a faint feature around 510 nm.

Silver based synthesis. The addition of silver precursor to the reaction did not initially translate into any visible effects, neither in the presence of CTAB/TMB nor after adding THPC. Nevertheless, after adding potassium carbonate to the silver based synthesis, the solution started to turn pale yellow within the first hour of reaction and resulted in an intense yellow coloration after 6 hours, at which point the TEM samples were prepared. This yellow coloration is classic for such small silver nanoparticles showing a surface plasmon resonance centered around 420 nm as shown in Extended Data Figure 8.

Vanadium oxide based synthesis. The vanadium oxide cage-like nanoparticles were prepared under the same conditions as the silicage, however the pH was not adjusted with ammonia due to the fast hydrolysis and condensation rate of the vanadium oxide precursor. In contrast to the metal cage-like nanoparticles synthesis, no alcohol was added here since the hydrolysis of the vanadium precursor, vanadium oxytriisopropoxide, produces alcohol similar to the silicage synthesis. The addition of this precursor to the TMB micelles resulted in the immediate formation of a red precipitate. Under stirring, the precipitate dispersed homogeneously in solution, which remained turbid, and turned orange after one day of reaction at 30 °C.

Data availability. The figures, which have associated raw data, include: Figures 2, 3, and 4, as well as Extended Data Figures 1, 2, 3, 4, 5c, 6, 7, 8, and 9. There are no restrictions on data availability. The datasets generated and analyzed during the current study are available from the corresponding author on reasonable requests.

Code availability. The custom code and algorithm used for the 3D reconstruction and related analysis during the current study are available from the corresponding author on reasonable requests.

Additional references

31. Westcott, S. L., Oldenburg, S. J., Lee, T. R. & Halas, N. J. Formation and Adsorption of Clusters of Gold Nanoparticles onto Functionalized Silica Nanoparticle Surfaces. *Langmuir* **14,** 5396–5401 (1998).

32. Ji, B. *et al.* Non-blinking quantum dot with a plasmonic nanoshell resonator. *Nat. Nanotechnol.* **10,** 170–175 (2015).

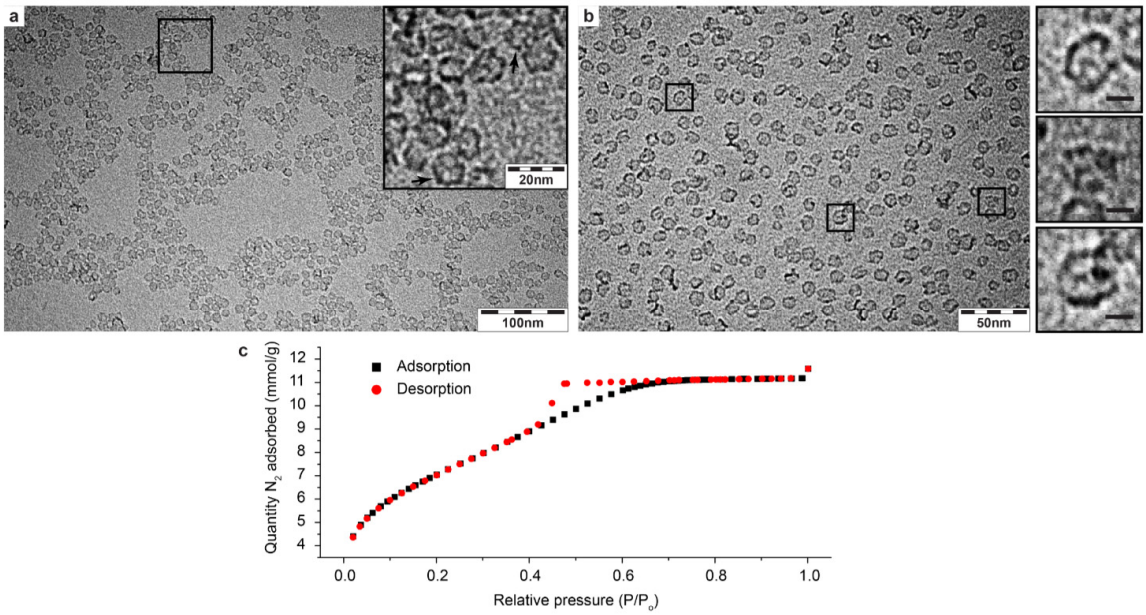

Extended Data Figure 1 | PEGylated silicages after cleaning and nitrogen sorption measurements on calcined cages. a and **b**, Representative dry-state TEM images at different magnifications of PEGylated silicages after the removal of surfactant and TMB (Methods section). Particles in (**a**) (inset, black arrows) as well as in the insets in (**b**) exhibit cage-like structure, suggesting structure preservation after the removal of CTAB and TMB. **c**, Nitrogen absorption and desorption isotherms of calcined silicages. After the removal of surfactant and TMB, particles were calcined at 550 °C for 6 hours in air prior to nitrogen sorption measurements. A particle synthesis yield of 67% was estimated from the weight of the calcined powder. The surface area of calcined silicages as assessed by the Brunauer–Emmett–Teller (BET) method was 570 m^2/g, consistent with theoretical estimations (Methods section). Scale bars in the insets in (**b**) are 5 nm.

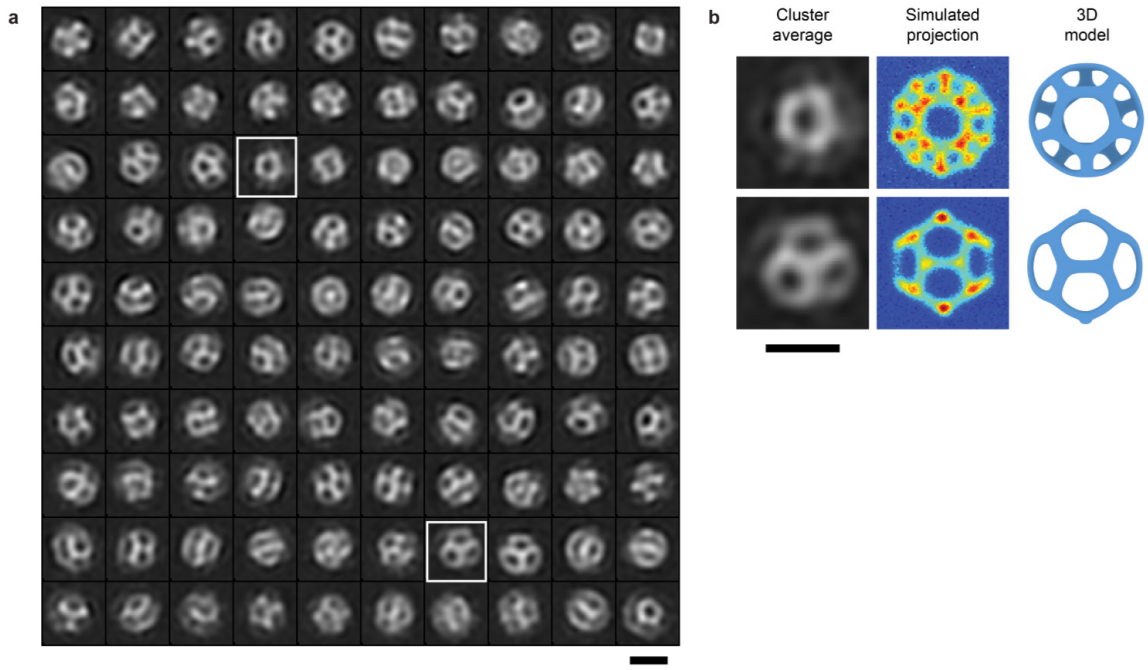

Extended Data Figure 2 | Cluster averages of 2D images of silicages. a, ~19,000 single particle cryo-EM images were sorted into 100 clusters[20]. **b**, Some of the projections (examples highlighted in **a**) exhibited features similar to projections of dodecahedral cage structure obtained by simulation. Also shown are projection models. The scale bars are 10 nm.

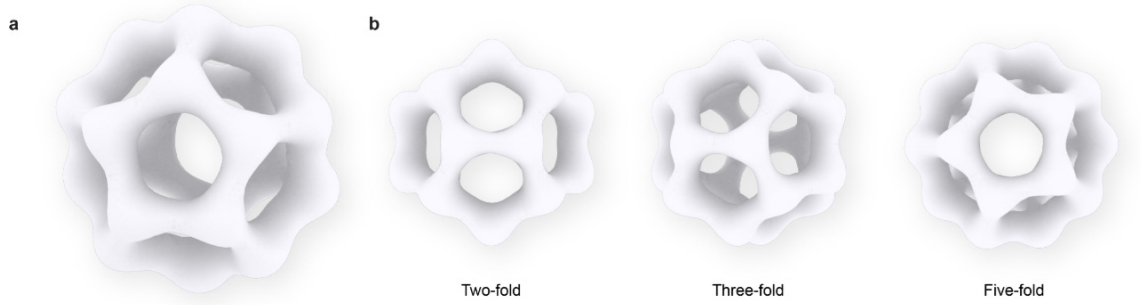

Extended Data Figure 3 | Reconstruction of silicage using RELION 2.1 system. Dodecahedral silicage reconstruction result[24] (**a**) and its three most unique projections along the two-, three- and five-fold symmetry axes (**b**). The reconstruction was obtained from a single-class calculation run by RELION 2.1 using the same set of single particle images as was used in the class of the dodecahedral cage shown in Figure 3a. Visualization is by UCSF Chimera[23].

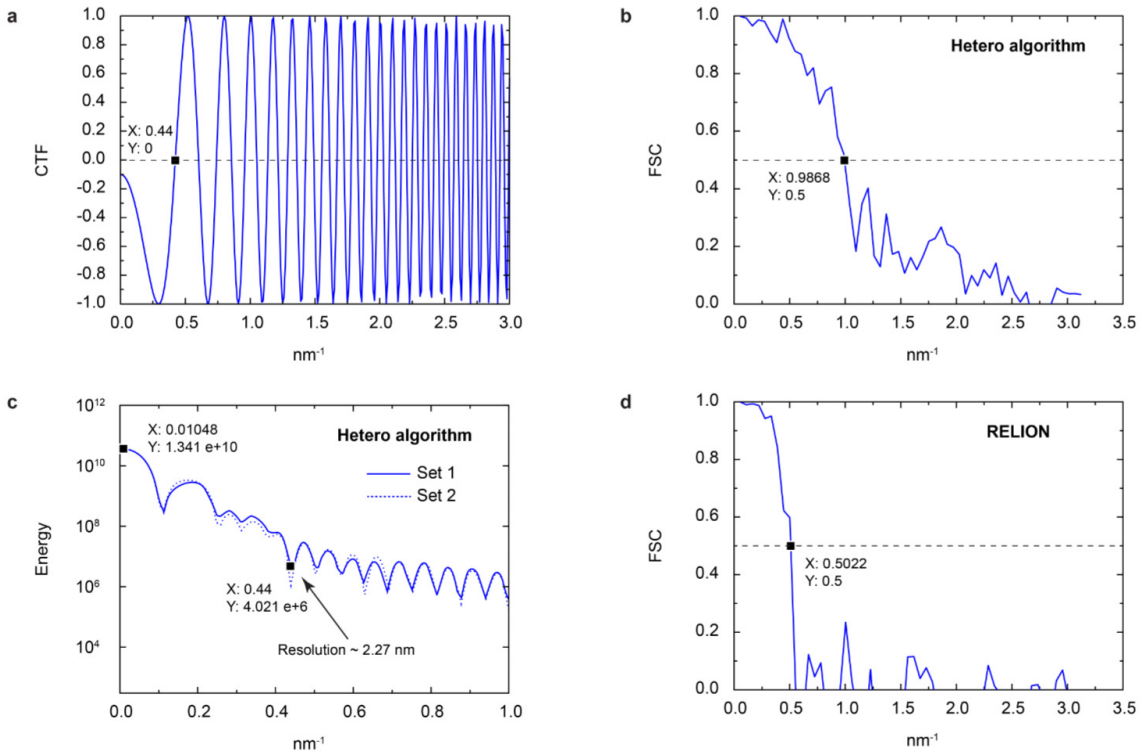

Extended Data Figure 4 | A typical CTF and determination of reconstruction resolution. CTFFIND4.1.8[26] was used to estimate defocus for individual micrographs or set of micrographs with results consistent with the nominal defocus values of 1 to 2 microns. **a**, Contrast transfer function (CTF) for defocus 1.98 microns. Since the first zero-crossing of CTF occurs at 0.44 nm^{-1}, the CTF has little effect on reconstructions unless the resolution is greater than 1/0.44 = 2.27 nm. **b**, Fourier Shell Correlation (FSC)[25] computed by standard package[20] for two Hetero reconstructions that are independent starting at the level of separate sets of images each containing 2000 images (*i.e.*, "gold standard" FSC). The resolution implied by the FSC curve (at 0.5 threshold) is 1/0.99 = 1.01 nm. **c**, Energy function for the same pair of reconstructions as in (**b**). Energy is the spherical average of the squared magnitude of the reciprocal-space electron scattering intensity, where the denominator of FSC is the square root of a product of two Energy functions, one for each reconstruction. The observations that Energy has dropped by more than 10^{-3} times its peak value and the character of the curve has become oscillatory and more slowly decreasing, both by 0.44 nm^{-1}, indicates that the resolution implied by the FSC curve (at 0.5 threshold) is exaggerated[22] and that a more conservative resolution is 1/0.44 = 2.27 nm. **d**, FSC computed by a standard package[20] for two RELION 2.1 reconstructions computed from the same images as the reconstructions in (**b**), from which the resolution (at 0.5 threshold) is estimated to be around 1/0.50 = 2.00 nm.

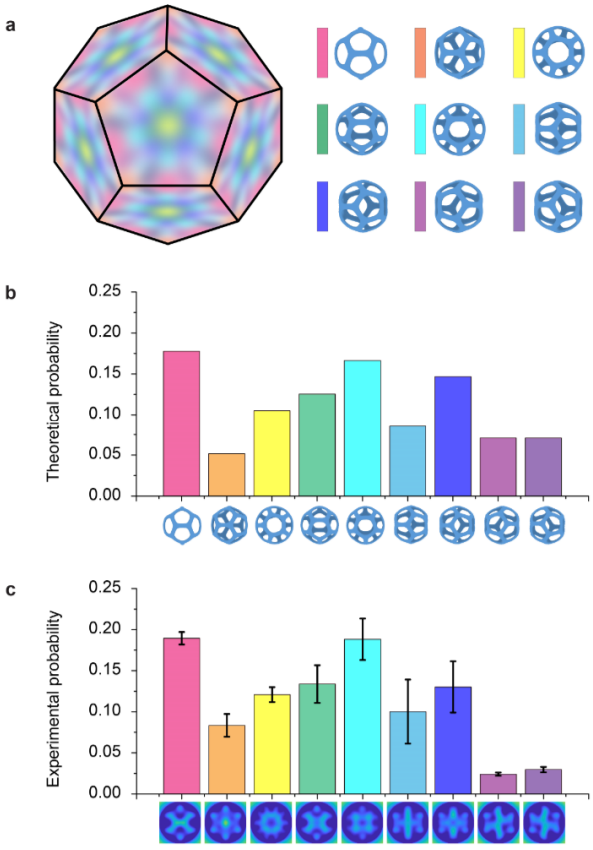

Extended Data Figure 5 | Probability analysis of silicage projections. a, Orientation dependence of silicage projections. The orientations, at which the nine different silicage projections (right panel) can be seen, are calculated, and manually mapped on a surface of a dodecahedron (left panel). The orientations, corresponding to different projections, are assigned to different colors. **b**, Probability analysis for different silicage projections. The probability of imaging a particular projection in EM is estimated by dividing that subset of the surface area of a sphere which contains the orientations that correspond to the specific projection, by the total surface area of the sphere (**a**). **c**, Experimental probability of different silicage projections. The probability of each projection is calculated by dividing the number of the single particle images assigned to the specific silicage projection via 3D reconstruction by the overall number of silicage single particle images. The error bars in (**c**) are standard deviations calculated from three projection distributions, which were obtained from three independent reconstruction runs using different sets of single particle images, respectively.

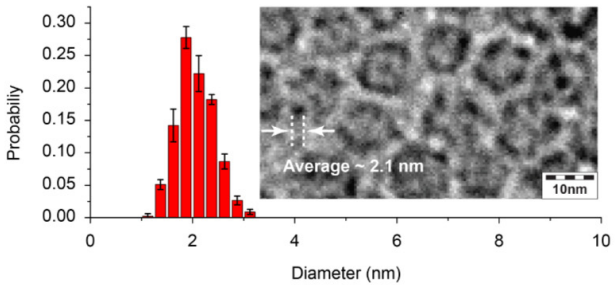

Extended Data Figure 6 | Size analysis of silica clusters at an early stage of cage formation. Particle size distribution for primary silica clusters at an early stage of cage formation, obtained by manually analyzing 450 silica clusters using a set of TEM images. The measured silica clusters were randomly split into three groups, each containing 150 particles. A cluster size distribution was then obtained for each of the three groups, respectively, and the results were averaged. The error bars are standard deviations calculated from the three cluster size distributions. A representative TEM image is included in the inset. In order to quench the very early stages of cage formation, PEG-silane was added into the synthesis mixture about three minutes after the addition of TMOS thereby PEGylating early silica structures. TEM sample preparation and characterization were as described before (Methods section). Primary silica clusters with diameters around 2 nm were identified, consistent with the proposed cage formation mechanism.

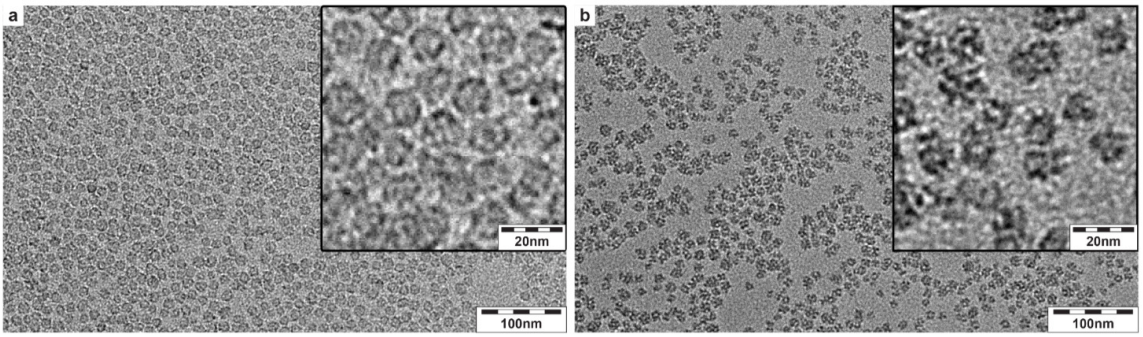

Extended Data Figure 7 | Role of TMB in cage formation. TEM images at different magnifications of silica nanoparticles that were synthesized with (**a**) and without (**b**) TMB. Nanoparticles synthesized without TMB (**b**) exhibited stronger contrast at the particle center as compared to the nanocages (**a**), suggesting that these particles did not exhibit hollow cage-like structures but instead were conventional mesoporous silica nanoparticles with relatively small particle sizes (**b**).

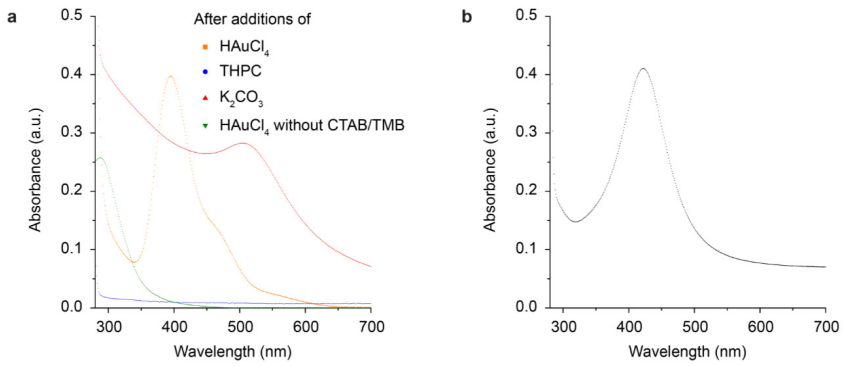

Extended Data Figure 8 | Optical characterization of gold and silver based synthesis solutions. a, Survey of the gold based synthesis showing the absorption profile of solutions after the successive additions of $HAuCl_4$ (orange), THPC (blue), one day after the addition of K_2CO_3 (red), and compared to the same concentration of $HAuCl_4$ added to the equivalent water/ethanol solution but without any CTAB or TMB (green). **b**, Absorption profile of a solution obtained from the silver synthesis 6 hours after the addition of K_2CO_3.

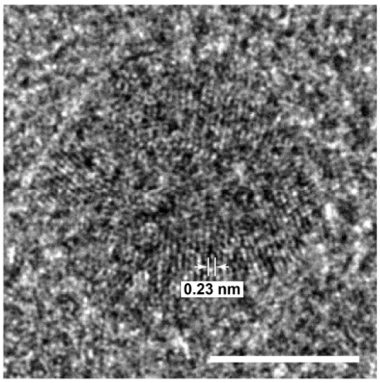

Extended Data Figure 9 | High resolution TEM image of single cage-like gold nanoparticle. The gold particle exhibited lattice fringes with a spacing of 2.3 Å, consistent with the lattice spacing between (111) planes of gold (JCPDS no. 04-0784). The scale bar is 5 nm.

Surfactant micelle self-assembly directed highly symmetric ultrasmall inorganic cages

Kai Ma[1], Yunye Gong[2], Tangi Aubert[1,3], Melik Z. Turker[1], Teresa Kao[1], Peter C. Doerschuk[2,4], Ulrich Wiesner[1]

[1]Department of Materials Science Engineering, Cornell University, Ithaca, NY 14853, USA.

[2] School of Electrical and Computer Engineering, Cornell University, Ithaca, NY, 14853, USA.

[3]Department of Chemistry, Ghent University, Ghent, 9000, Belgium.

[4]Nancy E. and Peter C. Meinig School of Biomedical Engineering, Cornell University, Ithaca, NY 14853, USA.

Correspondence to: Ulrich Wiesner (ubw1@cornell.edu)

Supplementary Information

The Supplementary Information includes two supplementary videos of the 3D reconstructions obtained using Hetero algorithm and RELION 2.1 system, respectively. Both of the videos are in mp4 format, and their captions are as the following:

Supplementary Video 1 | Reconstruction of silicage using Hetero algorithm. The reconstruction was obtained from a single-class calculation by the Hetero algorithm using the same set of single particle images as was used in the class of the dodecahedral cage shown in Figure 3a.

Supplementary Video 2 | Reconstruction of silicage using RELION 2.1 system. The reconstruction was obtained from a single-class calculation by the RELION 2.1 system using the same set of single particle images as was used in the class of the dodecahedral cage shown in Figure 3a.